Science and Technology Indonesia
e-ISSN:2580-4391 *p*-ISSN:2580-4405
Vol. 10, No. 3, July 2025

Research Paper

Influence of Mg Incorporation on the Structural and Electrochemical Properties of $LiMn_{1-x}Mg_xO_2$ Cathode Material for Lithium-Ion Batteries

Nour Abd Alrazaq Hassan[1*], Muhammad Hameed Al-Timmi[1]

[1]*Department of Physics, College of Science, University of Diyala, 32006, Iraq*
***Corresponding author**: nourabdalrazaq0@gmail.com

Abstract
In this study, the urea route technique was used to synthesize $LiMn_{1-x}Mg_xO_2$ compounds with (x = 0, 0.125, 0.25, 0.375, 0.5, 0.625, and 0.75 wt.%) as cathode active materials for lithium-ion batteries. All prepared samples underwent structural and morphological analysis. The X-ray diffraction (XRD) results showed a single-phase crystal structure for the synthesized nanoparticles. The crystalline size (D111) of the produced particles was calculated using Debye-Scherrer's equation, and the results indicated only a slight change in particle size upon substitution of magnesium ions. Fourier transform infrared spectroscopy (FTIR) analysis revealed several vibrational modes, including (O−H and C=O). Field emission scanning electron microscopy (FESEM) images also revealed that the nanoparticles were cubic, with little variation in size distribution. The synthesized $LiMn_{1-x}Mg_xO_2$ was further characterized by energy dispersive X-ray (EDX) spectroscopy. The findings confirmed the presence of magnesium (Mg), manganese (Mn), and oxygen (O). Electrochemical testing was conducted only on samples of $LiMn_{1-x}Mg_xO_2$ (x = 0, 0.125, and 0.75 wt.%). Electrochemical experiments showed that $LiMn_{1-x}Mg_xO_2$ (x = 0.125 and 0.75 wt.%) exhibited greater charge and discharge capacities than the $LiMnO_2$ electrode. These results were consistent with the findings from electrochemical impedance spectroscopy (EIS). Overall, the electrochemical experiments demonstrated that $LiMn_{1-x}Mg_xO_2$ (x = 0.125 and 0.75 wt.%) performed better than $LiMnO_2$.

Keywords
Urea Route Method, Structure Properties, CV, EIS, GCD, LIB

Received: 10 November 2024, Accepted: 2 May 2025
https://doi.org/10.26554/sti.2025.10.3.826-836

1. INTRODUCTION

Lithium-ion batteries (LIBs) have become the current industry leader due to several intrinsic qualities, including high specific capacity and voltage, high energy density, excellent cycle performance, low self-discharge rate, absence of memory effects, wide operating temperature range, and long service life. These characteristics make LIBs a superior power source compared to other types of batteries. Extensive research on both electrode components-anodes and cathodes-has led to enhanced performance and reduced manufacturing costs. As a result, LIBs are now widely used in various fields, including information technology, energy, transportation, new energy vehicles, and military applications (Goodenough, 2013; Yi, 2016; Kerista Tarigan, 2024; Almafie et al., 2024).

Currently, there is growing interest in hybrid electric vehicles (HEVs) and electric vehicles (EVs) due to their enhanced cruising range and extended travel distances (Scrosati and Garche, 2010; Sun et al., 2009). $LiCoO_2$, recognized as the first commercial cathode material, is primarily used in the computer, communication, and consumer electronics sectors due to its high cost (Ou et al., 2016). Although materials such as $LiFePO_4$ and $LiMnO_2$ (M= Ni, Co, Mn, etc.) are employed in EVs and HEVs, their theoretical capacities are insufficient to meet the requirements of high-power lithium-ion batteries (Wu et al., 2014; Yuan et al., 2011; Hakim and Pangestu, 2022).

Identifying cathode materials with greater competitiveness and robust discharge characteristics has become essential. Manganese based $LiMn_{1-x}Mg_xO_2$ has emerged as a promising candidate for cathodes in hybrid electric vehicles (HEVs) due to its low cobalt content and high theoretical specific capacity (up to 250 mAh/g) (Croy et al., 2013; He et al., 2015; Martha et al., 2012). However, major drawbacks of these cathode materials include severe discharge capacity fading, limited rate capability, and significant irreversible capacity loss during the first cycle (Gu et al., 2013; Li et al., 2012).

Due to their similar ionic radii, Li^+ and other ions such as Mn^{3+} (0.53 nm), Ni^{2+} (0.69 nm), Co^{3+} (0.685 nm), and Li^+ (0.76 nm) are prone to cation mixing, which is a primary factor contributing to poor electrochemical performance (van

Bommel et al., 2011; Hakim and Pangestu, 2022). Altering the composition and ion doping are among the most effective strategies for reducing cation mixing (Croy et al., 2012; Li et al., 2013). Considerable research has focused on modulation optimization due to its practicality and cost-effectiveness (Kong et al., 2013). Manganese-based layered lithium-rich oxides are commonly synthesized via co-precipitation methods because of their simplicity and efficiency (Ma et al., 2016; Zhu and Zhu, 2014).

$LiMnO_2$ distinct electronic structure and redox activity make it a promising material with significant potential. To fully harness the capabilities of $LiMn_{1-x}Mg_xO_2$, it is essential to develop nanostructures, as they exhibit superior properties compared to their bulk counterparts. This review highlights the importance of nanomaterials, with a focus on the synthesis methods and applications of $LiMnO_2$ nanostructures. Nanomaterials possess unique mechanical, chemical, and physical properties, making them highly attractive for a wide range of applications, including energy storage, catalysis, sensing, and medical technologies (Hakim and Pangestu, 2022).

$LiMnO_2$ nanostructures can be created using a variety of synthesis techniques, each of which has unique benefits in terms of control over size, shape, and crystallinity. These techniques include chemical vapor deposition (CVD), Urea route methods, template-assisted methods, and solvothermal/hydrothermal synthesis. In solvothermal/hydrothermal synthesis, precursor liquids are reacted with at high pressure and temperature to produce distinct nanostructures. Urea route techniques enable easy compositional adjustment and adding, as well as flexibility in precursor selection. Template-assisted methods give the produced nanostructures certain morphologies by using sacrificial templates. $LiMnO_2$ nanostructures with the required characteristics for specific applications can be created by adjusting the synthesis conditions and precursor chemistry (Homada et al., 2023).

In this study, a series of magnesium-doped samples, $LiMn_{1-x}Mg_xO_2$ (x = 0, 0.125, 0.25, 0.375, 0.5, 0.625, 0.75), were synthesized using the urea method. A detailed investigation was carried out to examine the effects of magnesium substitution on the structural properties, surface chemical states, and electrochemical performance of $LiMn_{1-x}Mg_xO_2$ for selected compositions (x = 0, 0.125, 0.75).

2. EXPERIMENTAL SECTION

2.1 Materials

The chemicals used in this investigation included manganese chloride tetrahydrate ($MnCl_2.4H_2O$, MW = 197.90 g/mol), citric acid (MW = 192.13 g/mol), nitric acid (HNO_3 70%), lithium chloride (LiCl, MW = 42.39 g/mol), and urea (NH_2CONH_2, MW = 60.06 g/mol). As precursors for lithium ions, stoichiometric amounts of manganese chloride ($MnCl_2.4H_2O$), lithium chloride (LiCl), and magnesium chloride hexahydrate ($MnCl_2.6H_2O$, MW = 203.30 g/mol) were used. It is crucial to ensure that all precursors are fully dissolved in distilled water and thoroughly mixed with continuous stirring. To prepare a preliminary 100 mL solution, the stock solution was carefully combined with an aqueous medium containing urea and citric acid ($C_6H_8O_7$). Table 1 provides a detailed overview of the materials used in this study.

Table 1. Shows the Materials used in the Research

Materials	Chemical Formula	Mw g/mol	Purity%	Supplier
Lithium chloride	LiCl	42.394	98%	Thomas Baker
Manganese II chloride	$MnCl_2.4H_2O$	197.90	98%	Alpha Chemical
Magnesium chloride	$MgCl_2.6H_2O$	203.30	98%	Alpha Chemical
Nitric acide	HNO_3	63.01	98%	Thomas Baker
Urea	CH_4N_2O	60.06	98%	Thomas Baker
Citric acid	$C_6H_8O_7$	192.124	99%	Thomas Baker

2.2 Procedures

2.2.1 The Cathode Material Preparation

The cathode materials were produced using the urea route method, which required maintaining metal ion equilibrium by setting the molar ratio of urea to total metal ions at 1:1, and citric acid to total metal ions at 1:2. The original solution was continuously stirred while nitric acid (HNO_3) was added at a molar ratio of 1:0.1. After thorough mixing, the solution was heated to 85°C for four hours, with intermittent breaks to facilitate the evaporation of residual water. As the viscosity increased, the solution gradually transformed into a dark resin, accompanied by intermittent foaming. The evaporation process was considered complete once a black gel was obtained.

The resulting resin was baked in an oven at 180°C for approximately six hours to ensure complete drying. During this process, the gel expanded to three to four times its original volume, forming polymerization intermediates. The dried material was then subjected to calcination at 800°C for four hours (Homada et al., 2023; Abdullah et al., 2019b).

Subsequently, different proportions of magnesium metal (0, 0.125, 0.25, 0.375, 0.5, 0.625, and 0.75 wt.%) were mixed with manganese metal (Mn:Mg). The structure and phase composition of the materials were analyzed using X-ray diffraction (XRD) with CuKα radiation, over a range of 10-90° with a scan time of 0.5 seconds and a step size of 0.02°. The CuKα radiation was removed during analysis. The Rietveld method, implemented via the X'Pert HighScore Plus software, was used to determine the structural and lattice parameters.

Infrared (IR) spectra of the samples were recorded. The morphology of the synthesized powders was examined using energy-dispersive X-ray (EDX) analysis, field emission scanning electron microscopy (FE-SEM), and Fourier-transform

Table 2. Shows the Devices used to Analyze the Prepared Materials

The Device's	Specification	The Company, and Model
X-ray diffraction (XRD)	1.5 Å diffractive meter from Cu Kα radiation. 2θ range: 10° to 90°. 2°/min is the scan rate. 40 KV of voltage. 30 mA of current. Ferdowsi University, Mashhad, Iran, Science Physics.	Shimadzu XRD-6000 (Japan)
Fourier Transform Infrared Spectroscopy (FTIR) for powder	Give molecular structures a range of mechanical and thermal characteristics. Triglycine sulfate (TSS) 350–7800 cm^{-1} and semiconductor-type detector MCT (Hg Cd Te) are the detectors.	Alpha from Bruker Optics (Germany)
Field Emission Scanning Electron Microscope (FE-SEM)	Characteristics of the terrain, including the particle sizes and shapes.	MIRA3 TESCAN
Energy Dispersive X-ray Spectroscopy (EDX)	Microstructure analysis. potential is up to 30 kV.	Screenshot showing 3D Tomography module. Tescan VegaIII ,Czech Republic, (USA)
Cyclic Voltammetry (CV)	The galvanostatic charge-discharge experiments were conducted using a Neware multi-channel instrument (CT-3008). The coin cells were analyzed at varying rates in a potential range of 2.0 to 4.8 V (versus Li $(Li^+)^{-1}$).	model CT_3008
Electrochemical Impedance Spectroscopy (EIS)	Data analysis software utilizing the fast computation speed of recent computers.	Model, WisEIS-8100 premium

infrared spectroscopy (FTIR, 1600 Series), along with room temperature thermocline analysis (Anexus). The software was also used to estimate the average particle size and provide microscopic illustrations of the particles.

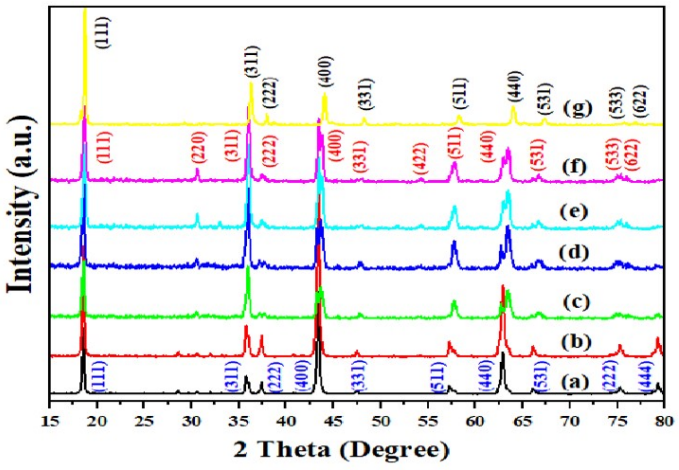

Figure 1. XRD Patterns of Prepared $LiMn_{1-x}Mg_xO_2$ Nanopowder at Different Mg Metal Ratios (a) $LiMnO_2$ (b) $LiMn_{0.875}Mg_{0.125}O_2$ (c) $LiMn_{0.75}Mg_{0.25}O_2$ (d) $LiMn_{0.625}Mg_{0.375}O_2$ (e) $LiMn_{0.5}Mg_{0.5}O_2$ (f) $LiMn_{0.375}Mg_{0.625}O_2$ (g) $LiMn_{0.25}Mg_{0.75}O_2$

2.2.2 Fabrication of Coin Cell

To produce the cathode, active nanomaterials and conductive carbon powder are mixed in a weight ratio of 85:15. To enhance adhesion, a small amount (5%) of polyvinylidene fluoride (PVDF) dissolved in N-methyl-2-pyrrolidone (NMP) is added to the mixture. This slurry is then coated onto an aluminum foil sheet. To ensure stability, the coated electrode is dried in a vacuum oven at 100°C for at least eight hours and subsequently pressed onto the aluminum surface. The electrolyte, lithium perchlorate ($LiClO_4$) salt, is anhydrous and stored in an oven at 90-120°C for 24 hours. After cooling, a 1 M solution is prepared using tetrahydrofuran ($C_4H_6O_3$) as the solvent.

The anode is fabricated from circular metal plates cut to the appropriate diameter. A porous polypropylene separator sheet (Selgard) is used to prevent short-circuiting by being placed between the electrodes after soaking in the electrolyte for 12 hours. The cathode is positioned and attached in the same manner on the opposing side of the polymeric assembly. All stages of the battery fabrication process-including Li coin cell assembly and component integration-are performed in an argon-filled glove box to maintain an inert atmosphere. The instruments used for analyzing the prepared materials are listed in Table 2.

The methodology used in this study was adapted from previously published techniques. Specifically, the experimental conditions and cyclic voltammetry setup were based on the work of Abdullah et al. (2019a) and Homada et al. (2023),

Table 3. The XRD Calculations of Synthesized $LiMn_{1-x}Mg_xO_2$ Samples

Sample	2θ (deg)	FWHM (deg)	Crystalline Size (nm)	(hkl)
$LiMnO_2$	18.27	0.2456	31.92	(111)
$LiMn_{0.875}Mg_{0.125}O_2$	18.27	0.30519	25.69	(111)
$LiMn_{0.75}Mg_{0.25}O_2$	18.41	0.2954	26.77	(111)
$LiMn_{0.625}Mg_{0.375}O_2$	18.47	0.2954	26.92	(111)
$LiMn_{0.5}Mg_{0.5}O_2$	18.51	0.28542	27.61	(111)
$LiMn_{0.375}Mg_{0.625}O_2$	18.54	0.2791	28.09	(111)
$LiMn_{0.25}Mg_{0.75}O_2$	18.67	0.25124	30.85	(111)

which provided a foundation for investigating related electrochemical systems. However, several modifications were made to optimize the process for this investigation, including adjustments to the potential range, scan rate, and electrolyte composition.

3. RESULTS AND DISCUSSION

3.1 X-Ray Diffraction (XRD)

Figure 1 shows the XRD spectra of synthesized $LiMnO_2$ at different magnesium metal contents (0, 0.125, 0.25, 0.375, 0.5, 0.625, and 0.75 wt.%) relative to the manganese metal (Mn:Mg). The obtained peaks at 2θ = 18.27°, 35.36°, 36.99°, 42.98°, 47.05°, 56.83°, 62.4°, 65.61°, 74.81°, and 78.78° correspond to the crystalline planes (111), (311), (222), (400), (331), (511), (440), (531), (222), and (444), respectively. These peaks are indicative of the formation of pure cubic-$LiMnO_2$ with a space group of Fd-3m (no. 227) and lattice parameters a = b = c = 8.4105 Å, $\alpha = \beta = \gamma = 90°$, as shown in Figure 1(a), which is consistent with the standard data (ICDD 00-054-0256).

The XRD results demonstrated that the preparation method used in this work resulted in obtaining a cubic phase of all synthesized $LiMn_{1-x}Mg_xO_2$ nanopowders. The crystallite size of the synthesized $LiMn_{1-x}Mg_xO_2$ at different magnesium contents was calculated using the most intense peak (111) of $LiMn_{1-x}Mg_xO_2$, applying Debye-Scherrer's equation (Abdullah et al., 2024). The results showed that pure $LiMnO_2$ exhibited the largest crystallite size (31.92 nm), whereas for $LiMn_{1-x}Mg_xO_2$, the crystallite size increased with the magnesium ratio (0.125, 0.25, 0.375, 0.5, 0.625, and 0.75 wt.%). This behavior indicated an inverse relationship between crystallite growth and nucleation rate with increasing temperature during the heat treatment (Li et al., 2018; Llusco et al., 2020; Xiang et al., 2014; Zhao et al., 2015; Chidouh et al., 2023). Table 3 presents the XRD parameters of the $LiMn_{1-x}Mg_xO_2$ samples.

3.2 FTIR (Fourier-Transforms Infrared Spectroscopy)

The FTIR spectra of the $LiMn_{1-x}Mg_xO_2$ nanopowder, which was calcined at 800°C and had varying Mg concentrations, are shown in Figure 2. The FTIR spectra display a peak at 1620 cm^{-1} and a noticeably broad peak centered at 3400 cm^{-1}. These bands correspond to the bending and stretching vibrations of the (−OH) bond, respectively. The broadness of the vibration band at 3400 cm^{-1} in the $LiMn_{1-x}Mg_xO_2$ spectra indicates significant hydrogen bonding between water molecules and the crystallite surface (Etacheri et al., 2012; Feng et al., 1993; Mohammad Shafiee et al., 2018; Nagappa and Chandrappa, 2007). Furthermore, two separate peaks are observed at 620 and 506 cm^{-1}, which are attributed to magnesium and manganese metal-oxide bonds. A change in peak intensity was also observed with increasing Mg ion content, due to the interaction of metal ions within the $LiMn_{1-x}Mg_xO_2$ structure.

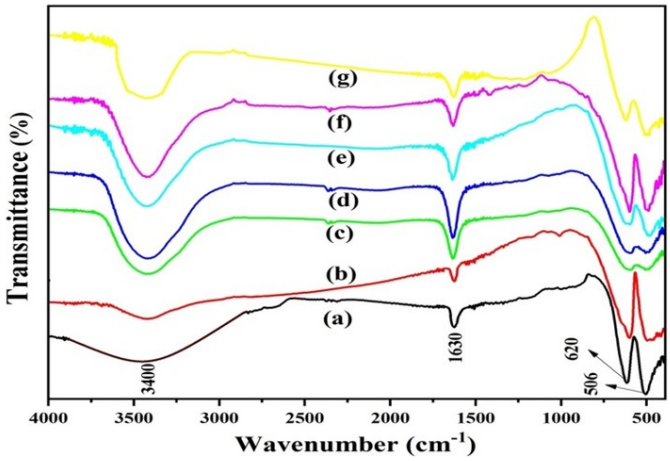

Figure 2. FTIR Spectra of Prepared $LiMn_{1-x}Mg_xO_2$ Nanopowder at Different Mg Metal Ratio (a) $LiMnO_2$ (b) $LiMn_{0.875}Mg_{0.125}O_2$ (c) $LiMn_{0.75}Mg_{0.25}O_2$ (d) $LiMn_{0.625}Mg_{0.375}O_2$ (e) $LiMn_{0.5}Mg_{0.5}O_2$ (f) $LiMn_{0.375}Mg_{0.625}O_2$ (g) $LiMn_{0.25}Mg_{0.75}O_2$

3.3 Morphological Studies

Field emission scanning electron microscopy (FE-SEM) was used to analyze the morphology of the composite powders. Additionally, energy dispersive X-ray analysis (EDX), also referred to as energy dispersive X-ray spectroscopy, is an X-ray technique used to determine a material's elemental composition or chemical characterization. Together with FE-SEM, EDX is employed to analyze the types and concentrations of

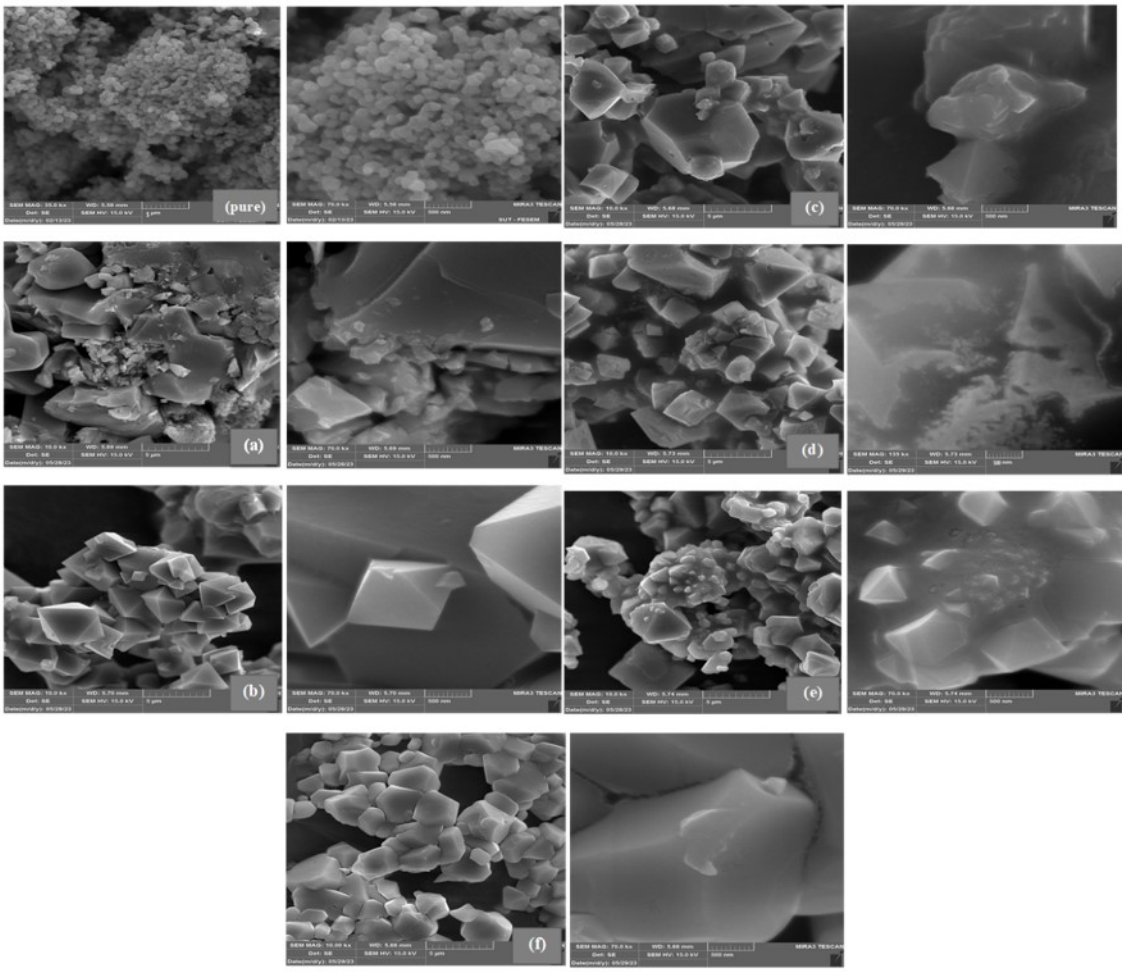

Figure 3. FESEM Micrographs of the (Pure) $LiMnO_2$ and $LiMn_{1-x}Mg_xO_2$ where (a) $LiMn_{0.875}Mg_{0.125}O_2$ (b) $LiMn_{0.75}Mg_{0.25}O_2$ (c) $LiMn_{0.625}Mg_{0.375}O_2$ (d) $LiMn_{0.5}Mg_{0.5}O_2$ (e) $LiMn_{0.375}Mg_{0.625}O_2$ (f) $LiMn_{0.25}Mg_{0.75}O_2$

elements present on or near the nanomaterial's surface, producing a detailed elemental map. Figure 3 presents the FE-SEM images of the synthesized $LiMn_{1-x}Mg_xO_2$ nanopowder at different Mg ratios (0.125, 0.25, 0.375, 0.5, 0.625, and 0.75 wt.%) at different scales (5 μm and 500 nm). The FE-SEM results indicated that the synthesized $LiMn_{1-x}Mg_xO_2$ (at all Mg ratios) has coarser particles compared to the pure $LiMnO_2$ nanoparticles. As shown in Figure 3 (a, b, c, d, e, and f), the FE-SEM results revealed that the produced $LiMn_{1-x}Mg_xO_2$ at various Mg ratios exhibited irregular shapes and strong, smooth aggregation, with an average particle size ranging from 120 nm to 140 nm. The higher amount of magnesium occupying the grain boundary zone within the pure $LiMnO_2$ structure is responsible for the larger average particle size, which influences the grain growth of the $LiMn_{1-x}Mg_xO_2$ product (Zipare et al., 2018).

The transport of matter between adjacent grains during the calcination process is linked to the microstructural properties and appearance of the prepared $LiMn_{1-x}Mg_xO_2$ (Banerjee et al., 2019). When doped with magnesium (Mg), it was observed that there was an increase in the irregularity of the shape of the $LiMn_{1-x}Mg_xO_2$ particles. This can be attributed to the gases released during the calcination process. The powders obtained after calcination were relatively fragile, which facilitated the grinding process and helped produce more distinct $LiMn_{1-x}Mg_xO_2$ particles (Dippong et al., 2019).

The characteristic peaks of manganese (Mn), magnesium (Mg), and oxygen (O)elements with weight ratios (Mn = 46.55 wt.%, Mg = 13.43 wt.%, and O = 68.18 wt.%) are displayed in the EDX results for the synthesized $LiMn_{1-x}Mg_xO_2$ (at an Mg ratio of 0.125 wt.%). As shown in Figure 4 and Table 4, increasing the Mg content leads to an increase in the weight (and atomic %) values of Mg, while the values for Mn decrease. The experimental weight (and atomic %) values closely matched the anticipated outcomes. The $LiMnO_2$ EDX spectra correlate well with the FE-SEM and XRD data. According to the obtained

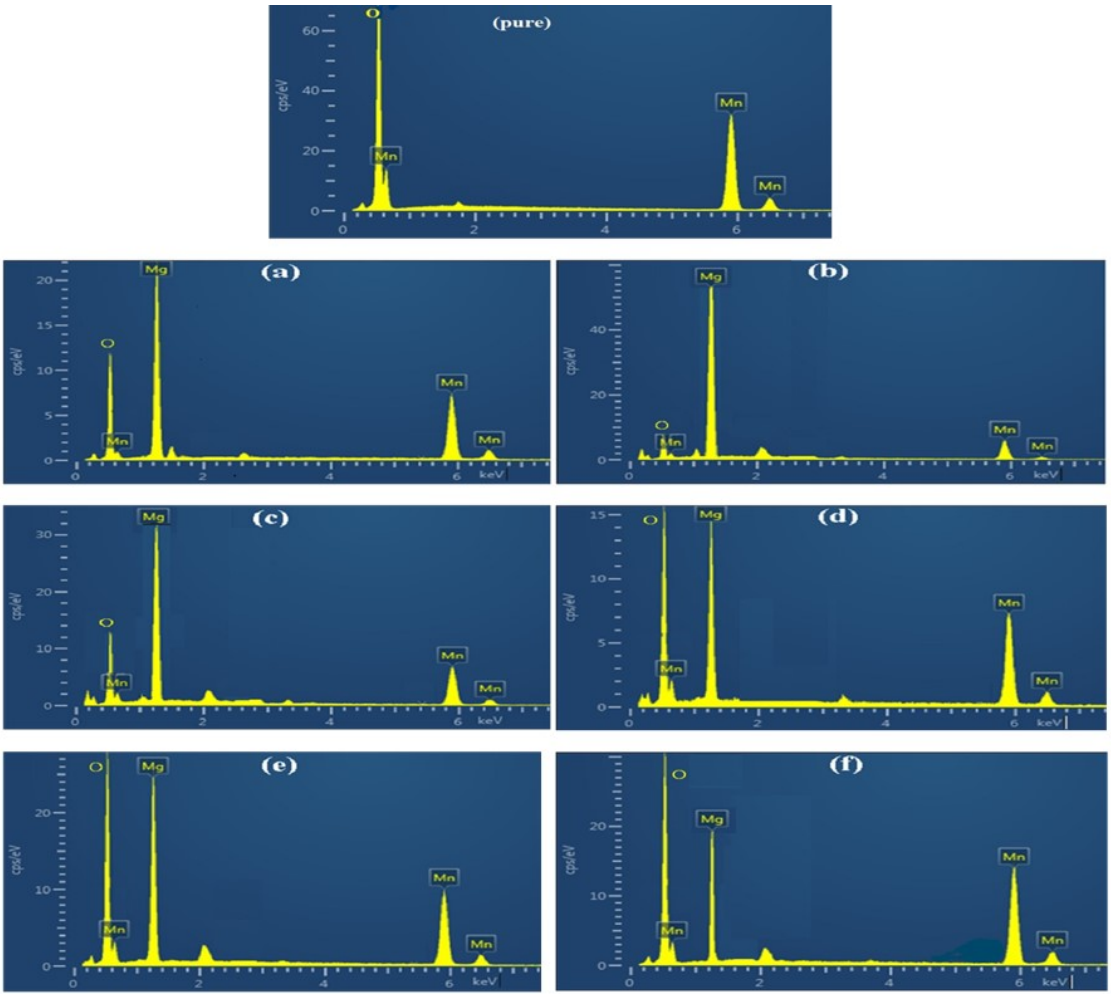

Figure 4. EDX Analysis of the $LiMnO_2$ (pure) and $LiMn_{1-x}Mg_xO_2$ Where (a) $LiMn_{0.875}Mg_{0.125}O_2$ (b) $LiMn_{0.75}Mg_{0.25}O_2$ (c) $LiMn_{0.625}Mg_{0.375}O_2$ (d) $LiMn_{0.5}Mg_{0.5}O_2$ (e) $LiMn_{0.375}Mg_{0.625}O_2$ (f) $LiMn_{0.25}Mg_{0.75}O_2$

EDX spectra, no additional contaminant peaks were observed in the final product. The EDX results of all samples showed the absence of a lithium characteristic peak, which is attributed to the lightweight nature of the lithium element (Ren et al., 2012).

3.4 Electrochemical Properties

For electrode preparation, cell formation, and sealing, an argon-filled glove box (MBRAUN-MB 200G) was used, with the oxygen content kept below 1.0 ppm. The positive electrode was made by combining 70% active material, 15% polyvinylidene difluoride (PVDF) binder, and 15% acetylene black in N-methyl-2-pyrrolidone (NMP) solvent. A mixed slurry diluted in NMP was uniformly applied on one side of aluminum foil with a known weight using a doctor's blade. The foil was then dried for 24 hours at 140°C in a vacuum oven. Afterward, the foil containing the paste was wrapped and allowed to dry for an additional two hours. The mass of the active material (cathode) was determined by comparing the weights of the paste-coated foil and the aluminum foil (Singh et al., 2010; Abdullah et al., 2019a). In the Teflon cell used for electrochemical testing, a small piece of lithium foil served as the negative electrode. A 1 M solution of $LiPF_6$ dissolved in a 1:1 volume mixture of ethylene carbonate and diethyl carbonate was used as the electrolyte, and polypropylene sheets were used as the separators. A computer-controlled system, operating between 2.0 and 4.8 V with a steady current of 100 mA at 20°C, was used to evaluate the cell (Lazanas and Prodromidis, 2023; Rohendi et al., 2023).

3.4.1 Cycle Voltammetry (CV)

Cyclic voltammetry (CV) is a powerful method commonly used to study the formation of biofilms and the effects of biocorrosion. The CV technique monitors the current passing through the working electrode by linearly increasing and decreasing its potential. CV is a practical technique for electrochemically examining deposits on conductive electrodes and traces of chemicals in water. This methodology offers a simple

Table 4. The Chemical Elements Ratio of Prepared $LiMn_{1-x}Mg_xO_2$ Nanopowder at Different Mg Ratios

Element	Weight (%)	Atomic (%)	Element	Weight (%)	Atomic (%)
$LiMn_{0.875}Mg_{0.125}O_2$			$LiMn_{0.5}Mg_{0.5}O_2$		
O	40.02	39.93	O	42.15	41.22
Mn	46.55	43.45	Mn	30.12	32.14
Mg	13.43	16.62	Mg	27.73	26.64
Total	100.00	100.00	Total	100.00	100.00
$LiMn_{0.75}Mg_{0.25}O_2$			$LiMn_{0.375}Mg_{0.625}O_2$		
O	42.21	43.65	O	39.55	40.07
Mn	38.24	39.45	Mn	22.48	21.78
Mg	19.55	16.90	Mg	37.97	38.15
Total	100.00	100.00	Total	100.00	100.00
$LiMn_{0.625}Mg_{0.375}O_2$			$LiMn_{0.25}Mg_{0.75}O_2$		
O	43.57	41.57	O	38.45	37.88
Mn	32.87	33.25	Mn	15.38	16.54
Mg	23.56	25.18	Mg	46.17	45.58
Total	100.00	100.00	Total	100.00	100.00

approach to corrosion investigation and biofilm measurement. Cyclic voltammetry is also a valuable technique for analyzing redox processes in energy storage and conversion devices such as fuel cells, supercapacitors, and lithium-ion batteries (LIBs) (Kissinger and Heineman, 1983; Abdullah et al., 2019b). Figure 5 shows the CV curve for $LiMnO_2$ produced using the urea route technique. Two anodic peaks at 4.12 and 4.28 V are visible in the $LiMnO_2$ sample, indicating that Mn^{3+} is oxidized to Mn^{4+} during the lithium removal (charging) process. Additionally, two cathodic peaks at 4.085 and 4.23 V are visible, suggesting that Mn^{4+} is reduced to Mn^{3+} during the lithium insertion (discharging) process. The presence of two distinct redox (oxidation and reduction) peaks indicates complex redox processes, possibly caused by structural alterations or multiple reaction mechanisms during the cycle. Alternatively, it can be inferred that both peaks are due to Li+ ions intercalating or deintercalating into or out of the cathode material (Ma et al., 2024).

Since Mg^{2+} is electrochemically inert, the $LiMn_{0.25}Mg_{0.75}O_2$ sample has two redox peaks at 4.089 and 4.218 V, indicating significant redox activity of Mn^{3+}/Mn^{4+}. Due to the inactivity of the magnesium ions, it also exhibits two cathodic peaks at 3.904 and 4.079 V, which demonstrate delayed reaction kinetics.

Two anodic peaks at 4.0 and 4.214 V demonstrate a balance between oxidation-reduction activity and stability in the $LiMn_{0.875}Mg_{0.125}O_2$ sample, while two cathodic peaks at 3.907 and 4.075 V, with a smaller ΔV compared to the sample with a higher magnesium concentration, show better charge transfer kinetics. The modest concentration of magnesium ensures structural integrity without significantly hindering the oxidation-reduction action. The process of lithium ion insertion or extraction into the electrode is also closely associated with each of the oxidation and reduction peaks displayed in the graphs (Parajuli and Murali, 2024; Wang et al., 2015; Abdullah et al., 2019a).

3.4.2 Charge and Discharge Cycles

Figure 6 shows the voltage vs. charge and discharge capacity curves for $LiMn_{1-x}Mg_xO_2$ (x = 0, 0.125, and 0.75) over the voltage range of 2 to 4.8V. The $LiMn_{1-x}Mg_xO_2$ concentration curves in the voltage range of 2 to 4.8V as a function of charge and discharge are shown for (x = 0, 0.125, and 0.75). The stability of the cubic transition within the crystal structure improves when magnesium is added to $LiMnO_2$. As the compound's magnesium concentration increases, the potential at 4.8V decreases, eventually disappearing entirely at (x = 0.125). $LiMnO_2$ has a discharge capacity of about 120.5 mAh/g. With an increase in magnesium content, there is a corresponding decrease in the capacitance of samples that contain magnesium (Singh et al., 2010). Due to its maximum charge capacity, discharge capacity, and Coulombic efficiency, the $LiMn_{0.25}Mg_{0.75}O_2$ sample performed the best. This suggests minimal energy loss throughout the charge-discharge cycle. Furthermore, the addition of magnesium (Mg) increases ionic transport efficiency and crystal structure stability. Magnesium ions form pathways that facilitate the movement of lithium ions within the electrode, improving the electrode's electrical conductivity and reducing polarization and charge transfer resistance. Additionally, using magnesium instead of lithium promotes more effective diffusion of lithium ions across the electrode (Parajuli and Murali, 2024; Wang et al., 2015; Abdullah et al., 2019a; Homad et al., 2024).

3.4.3 Stability Percentage

For $LiMnO_2$, $LiMn_{0.875}Mg_{0.125}O_2$, and $LiMn_{0.25}Mg_{0.75}O_2$, the discharge capacity versus cycle number is displayed in Figure 7 at a fixed current of 100 mA and a cutoff voltage be-

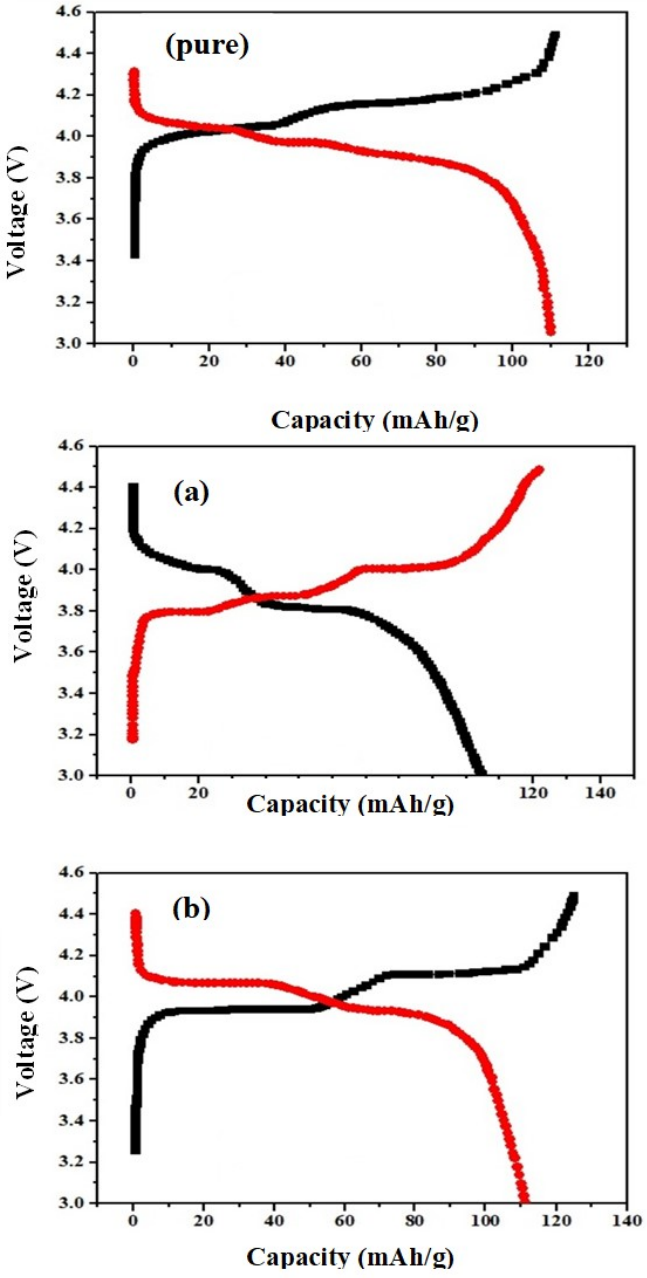

Figure 5. The CV at a Scan Rate of 1 mV s^{-1} in 2.0 to 4.8 V for: (pure) $LiMnO_2$, (a) $LiMn_{0.875}Mg_{0.125}O_2$, and (b) $LiMn_{0.25}Mg_{0.75}O_2$

tween 2.0 and 4.8 V. As the number of cycles increases, the capacity retention rate of the pure $LiMnO_2$, , and sample decreases, reaching 57.16% after 100 cycles. This suggests that the structure is not stable over the cycles, which is commonly attributed to structural distortions caused by the Jahn-Teller phenomenon and the formation of undesired phases during use. When magnesium is added, the $LiMn_{0.875}Mg_{0.125}O_2$ sample retains 67.49% of its initial capacity. Magnesium enhances structural stability. Further improvement is observed in the $LiMn_{0.25}Mg_{0.75}O_2$ sample, which shows a capacity retention of 76.91%. However, excessive replacement of magnesium may lead to a decrease in electronic conductivity, limiting further improvements (Singh et al., 2010).

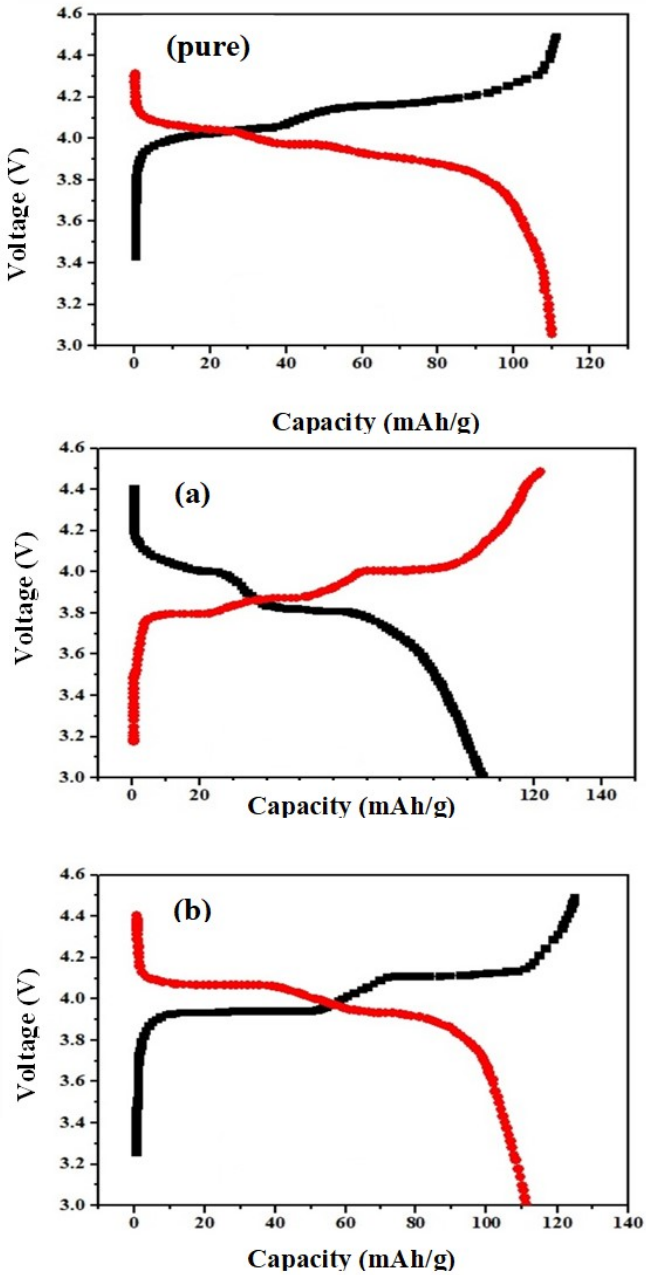

Figure 6. The Charge and Discharge Curves for: (Pure) $LiMnO_2$, (a) $LiMn_{0.875}Mg_{0.125}O_2$, and (b) $LiMn_{0.25}Mg_{0.75}O_2$

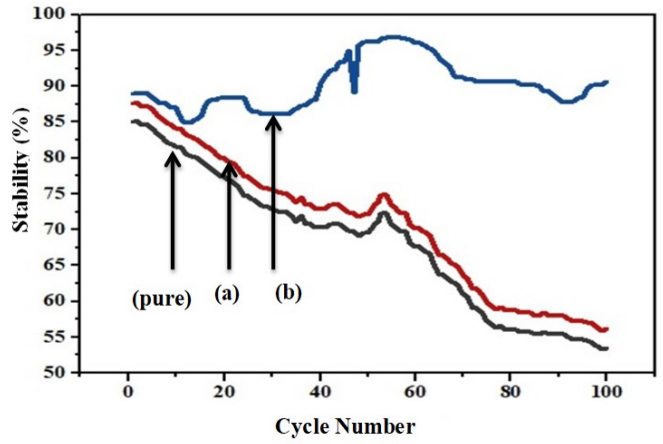

Figure 7. Stability Ratio Versus Cycle Number of: (Pure) $LiMnO_2$, (a) $LiMn_{0.875}Mg_{0.125}O_2$, and (b) $LiMn_{0.125}Mg_{0.75}O_2$ Cathode Materials

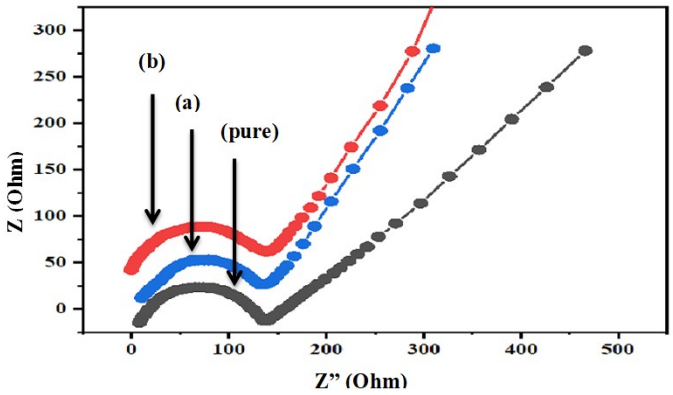

Figure 8. The Nyquist Plots of the Electrodes for: (Pure) $LiMnO_2$, (a) $LiMn_{0.875}Mg_{0.125}O_2$, and (b) $LiMn_{0.25}Mg_{0.75}O_2$

3.4.4 Electrochemical Impedance Spectroscopy (EIS)

Figure 8 displays the electrochemical impedance spectroscopy (EIS) curves for $LiMnO_2$, $LiMn_{0.875}Mg_{0.125}O_2$, and $LiMn_{0.25}Mg_{0.75}O_2$. The Nyquist plots of the cathode materials are shown in the figure. The kinetics of the electrochemical reactions occurring in the positive electrode and the charge transfer resistance (Rct) between the cathode and electrolyte are significant factors influencing the semicircular transition from medium to low frequency. The mobility of Li^+ ions in the bulk of the cathode material is associated with the linear relationship displayed by the Warburg impedance (W_o) (Shim et al., 2014; Homad et al., 2024). It was found that the $LiMnO_2$ electrode had a charge transfer resistance of 83.05 Ω, an electrolyte bulk resistance of 8.1 Ω, and a Warburg impedance of 0.12 Ω. In comparison to the $LiMnO_2$ electrodes, the $LiMn_{0.875}Mg_{0.125}O_2$ and $LiMn_{0.25}Mg_{0.75}O_2$ cathode materials demonstrated reduced Warburg impedance and charge transfer resistance. Since these samples showed good application effectiveness, chemical stability, and interaction with additives, $LiMn_{0.875}Mg_{0.125}O_2$, the best of the six compounds synthesized, has a smaller crystalline size than $LiMn_{0.25}Mg_{0.75}O_2$ (Abou-Rjeily et al., 2020).

4. CONCLUSIONS

The urea route approach was used to prepare $LiMn_{1-x}Mg_xO_2$ nanoparticles, which were subsequently calcined for four hours at 800°C. The effective incorporation of magnesium ions into the $LiMnO_2$ lattice was further confirmed by structural characterization and X-ray diffraction investigations. Additionally, crystal Mg metal was added to the synthesized $LiMnO_2$ nanostructures to decrease their size. The crystallite sizes of these nanoparticles fall within the nanometer range. FTIR analysis provides crucial details about a material's chemical bonding, which aids in understanding its composition. All samples exhibited nanostructural dimensions, according to FE-SEM analysis; nonetheless, EDX verified the elemental composition of the synthesized compounds. It is important to note that the quantity and quality of additives have a significant influence on each of these factors. These findings substantially enhance our understanding of the properties and potential applications of these materials in various fields, such as energy storage and catalysis.

5. ACKNOWLEDGEMENT

The facilities and assistance required for this study were provided by the University of Diyala, College of Science, Department of Physics, to which the authors are grateful. We also wish to express our gratitude to the laboratory personnel who assisted us in putting it into practice.

REFERENCES

Abdullah, H. W., T. H. Mubarak, and K. K. Resan (2024). Graphene Oxide Nano-Sheets: A Novel Eco-Friendly Approach for Tissue Engineering and Antibacterial Applications in Bone Disease. *Science and Technology Indonesia*, **9**(4); 806–817

Abdullah, M. Z., M. H. Al-Timimi, W. H. Albanda, M. Dumitru, A. E. Balan, C. Ceaus, and I. Stamatin (2019a). Structural and Electrochemical Properties of P3-$Na_{0.67}Mn_{0.3}Co_{0.7}O_2$ Nanostructures Prepared by Citric-Urea Self-Combustion Route as Cathode for Sodium Ion Battery. *Digest Journal of Nanomaterials and Biostructures*, **14**(4); 1179–1193

Abdullah, M. Z., H. M. Hasan, M. H. Al-Timimi, W. H. Albanda, M. K. Alhussainy, and M. Dumitru (2019b). Preparation and Characterization of Carbon Doped Lithium Iron Phosphate Composite as Cathode for Rechargeable Battery. *Journal of Ovonic Research*, **15**(3); 199–204

Abou-Rjeily, J., I. Bezza, N. A. Laziz, C. Autret-Lambert, M. T. Sougrati, and F. Ghamouss (2020). High-Rate Cyclability and Stability of $LiMn_2O_4$ Cathode Materials for Lithium-

Ion Batteries from Low-Cost Natural $\beta-MnO_2$. *Energy Storage Materials*, **26**; 423–432

Almafie, M. R., R. Dani, R. Riyanto, L. Marlina, J. Jauhari, and I. Sriyanti (2024). Preparation of PAN/PVDF Nanofiber Mats Loaded with Coconut Shell Activated Carbon and Silicon Dioxide for Lithium-Ion Battery Anodes. *Science and Technology Indonesia*, **9**(2); 427–447

Banerjee, S., P. C. Chakraborti, and S. K. Saha (2019). An Automated Methodology for Grain Segmentation and Grain Size Measurement from Optical Micrographs. *Measurement*, **140**; 142–150

Chidouh, A., T. Tahraoui, and B. Barhouchi (2023). Co-precipitation Synthesis and Antimicrobial Effect Study of Europium Doped Spinel Manganese Ferrites Nanoparticles ($MnEu_{0.1}Fe_{1.9}O_4$NPs). *Science and Technology Indonesia*, **8**(3); 494–500

Croy, J. R., K. G. Gallagher, M. Balasubramanian, Z. Chen, Y. Ren, D. Kim, S.-H. Kang, D. W. Dees, and M. M. Thackeray (2013). Examining Hysteresis in Composite $x\,Li_2MnO_3{\cdot}(1{-}x)\,LiMO_2$ Cathode Structures. *The Journal of Physical Chemistry C*, **117**(13); 6525–6536

Croy, J. R., D. Kim, M. Balasubramanian, K. Gallagher, S.-H. Kang, and M. M. Thackeray (2012). Countering the Voltage Decay in High Capacity $xLi_2MnO_3{\cdot}(1{-}x)\,LiMO_2$ Electrodes (M = Mn, Ni, Co) for Li^+-Ion Batteries. *Journal of the Electrochemical Society*, **159**(6); A781

Dippong, T., I. G. Deac, O. Cadar, E. A. Levei, L. Diamandescu, and G. Borodi (2019). Effect of Zn Content on Structural, Morphological and Magnetic Behavior of $Zn_xCo_{1-x}Fe_2O_4/SiO_2$ Nanocomposites. *Journal of Alloys and Compounds*, **792**; 432–443

Etacheri, V., R. Roshan, and V. Kumar (2012). Mg-Doped ZnO Nanoparticles for Efficient Sunlight-Driven Photocatalysis. *ACS Applied Materials & Interfaces*, **4**(5); 2717–2725

Feng, Q., Y. Miyai, H. Kanoh, and K. Ooi (1993). Li^+ and Mg^{2+} Extraction and Li^+ Insertion Reactions with $LiMg_{0.5}Mn_{1.5}O_4$ Spinel in the Aqueous Phase. *Chemistry of Materials*, **5**(3); 311–316

Goodenough, J. B. (2013). Evolution of Strategies for Modern Rechargeable Batteries. *Accounts of Chemical Research*, **46**(5); 1053–1061

Gu, M., I. Belharouak, J. Zheng, H. Wu, J. Xiao, A. Genc, K. Amine, S. Thevuthasan, D. R. Baer, and J.-G. Zhang (2013). Formation of the Spinel Phase in the Layered Composite Cathode Used in Li-Ion Batteries. *ACS Nano*, **7**(1); 760–767

Hakim, M. S. and H. Pangestu (2022). Preparation and Application of Nickel Electroplating on Copper (Ni/EC) Electrode for Glucose Detection. *Science and Technology Indonesia*, **7**(2); 208–212

He, F., X. Wang, C. Du, A. P. Baker, J. Wu, and X. Zhang (2015). The Effect of Samaria Doped Ceria Coating on the Performance of $Li_{1.2}Ni_{0.13}Co_{0.13}Mn_{0.54}O_2$ Cathode Material for Lithium-Ion Battery. *Electrochimica Acta*, **153**; 484–491

Homad, H., N. Ali, O. Al-Jubouri, M. Al-Timimi, and B. Abbas (2024). Synthesis of $LiCo_{1-x}Ni_xO_2$ Nanomaterial by Hydrothermal Method as Cathode for Lithium Ion Battery. *EUREKA: Physics and Engineering*, (4); 160–172

Homada, H. T., N. M. Alia, O. A. Al-Jubourib, and M. H. Al-Timimia (2023). Synthesis and Characterization of $LiCo_{1-x}Ni_xO_2$ Nanoparticles by Urea Route as Cathode for Lithium-Ion Battery. *Journal of Ovonic Research*, **19**(6); 783–791

Kerista Tarigan, E. A. M. S. F. J. P. Y. G. O. M., Riksson Siburian (2024). Fabrication and Optimization of Primary Batteries Using Ni/Graphene NanosheetElectrodes. *Science and Technology Indonesia*, **9**(2); 413–426

Kissinger, P. T. and W. R. Heineman (1983). Cyclic Voltammetry. *Journal of Chemical Education*, **60**(9); 702

Kong, J.-Z., X.-Y. Yang, H.-F. Zhai, C. Ren, H. Li, J.-X. Li, Z. Tang, and F. Zhou (2013). Synthesis and Electrochemical Properties of Li-Excess $Li_{1+x}[Ni_{0.5}Co_{0.2}Mn_{0.3}]O_2$ Cathode Materials Using Ammonia-Free Chelating Agent. *Journal of Alloys and Compounds*, **580**; 491–496

Lazanas, A. C. and M. I. Prodromidis (2023). Electrochemical Impedance Spectroscopy-A Tutorial. *ACS Measurement Science Au*, **3**(3); 162–193

Li, G., X. Feng, Y. Ding, S. Ye, and X. Gao (2012). AlF_3-Coated $Li(Li_{0.17}Ni_{0.25}Mn_{0.58})O_2$ as Cathode Material for Li-Ion Batteries. *Electrochimica Acta*, **78**; 308–315

Li, G., Y. Yu, T. Feng, M. Shao, C. Su, and J. Guo (2018). Study on Electrochemical Performance of $LiMg_{0.06}Mn_{1.94}O_4$ Synthesized by Solid-State Combustion Method. *International Journal of Electrochemical Science*, **13**(2); 1495–1504

Li, N., R. An, Y. Su, F. Wu, L. Bao, L. Chen, Y. Zheng, H. Shou, and S. Chen (2013). The Role of Yttrium Content in Improving Electrochemical Performance of Layered Lithium-Rich Cathode Materials for Li-Ion Batteries. *Journal of Materials Chemistry A*, **1**(34); 9760–9767

Llusco, A., M. Grageda, and S. Ushak (2020). Kinetic and Thermodynamic Studies on Synthesis of Mg-Doped $LiMn_2O_4$ Nanoparticles. *Nanomaterials*, **10**(7); 1409

Ma, J., T. Liu, J. Ma, C. Zhang, and J. Yang (2024). Progress, Challenge, and Prospect of $LiMnO_2$: An Adventure Toward High-Energy and Low-Cost Li-Ion Batteries. *Advanced Science*, **11**(2); 2304938

Ma, S., X. Hou, Z. Lin, Y. Huang, Y. Gao, S. Hu, and J. Shen (2016). One-Pot Facile Co-Precipitation Synthesis of the Layered $Li_{1+x}(Mn_{0.6}Ni_{0.2}Co_{0.2})_{1-x}O_2$ as Cathode Materials with Outstanding Performance for Lithium-Ion Batteries. *Journal of Solid State Electrochemistry*, **20**; 95–103

Martha, S. K., J. Nanda, G. M. Veith, and N. J. Dudney (2012). Electrochemical and Rate Performance Study of High-Voltage Lithium-Rich Composition: $Li_{1.2}Mn_{0.525}Ni_{0.175}Co_{0.1}O_2$. *Journal of Power Sources*, **199**; 220–226

Mohammad Shafiee, M. R., M. Kargar, and M. Ghashang (2018). Characterization and Low-Cost, Green Synthesis

of Zn^{2+} Doped MgO Nanoparticles. *Green Processing and Synthesis*, **7**(3); 248–254

Nagappa, B. and G. Chandrappa (2007). Mesoporous Nanocrystalline Magnesium Oxide for Environmental Remediation. *Microporous and Mesoporous Materials*, **106**(1–3); 212–218

Ou, J., L. Yang, and X. Xi (2016). Flour-Assisted Simple Fabrication of $LiCoO_2$ with Enhanced Electrochemical Performances for Lithium Ion Batteries. *Journal of Materials Science: Materials in Electronics*, **27**; 9008–9014

Parajuli, D. and N. Murali (2024). Mg^{2+} Substitution Effect on the Electrochemical Performance of $LiNi_{0.8-x}Mg_xCo_{0.1}Mn_{0.1}O_2$ (x = 0.00–0.05) Cathode Materials for LIBs. *AIP Advances*, **14**(8)

Ren, Y., J. Zhang, Y. Liu, H. Li, H. Wei, B. Li, and X. Wang (2012). Synthesis and Superior Anode Performances of TiO_2–Carbon–rGO Composites in Lithium-Ion Batteries. *ACS Applied Materials & Interfaces*, **4**(9); 4776–4780

Rohendi, D., N. F. Sya'baniah, E. H. Majlan, N. Syarif, A. Rachmat, D. H. Yulianti, and R. W. H. Erliana (2023). The Electrochemical Conversion of CO_2 into Methanol with $KHCO_3$ Electrolyte Using Membrane Electrode Assembly (MEA). *Science and Technology Indonesia*, **8**(4); 632–639

Scrosati, B. and J. Gar-che (2010). Lithium Batteries: Status, Prospects and Future. *Journal of Power Sources*, **195**(9); 2419–2430

Shim, J.-H., S. Lee, and S. S. Park (2014). Effects of MgO Coating on the Structural and Electrochemical Characteristics of $LiCoO_2$ as Cathode Materials for Lithium Ion Battery. *Chemistry of Materials*, **26**(8); 2537–2543

Singh, P., A. Sil, M. Nath, and S. Ray (2010). Synthesis and Characterisation of $Li[Mn_{2-x}Mg_x]O_4$ (x = 0.0–0.3) Prepared by Sol-Gel Synthesis. *Ceramics-Silikáty*, **54**(1); 38–46

Sun, Y.-K., S.-T. Myung, B.-C. Park, J. Prakash, I. Belharouak, and K. Amine (2009). High-Energy Cathode Material for Long-Life and Safe Lithium Batteries. *Nature Materials*, **8**(4); 320–324

van Bommel, A., L. Krause, and J. Dahn (2011). Investigation of the Irreversible Capacity Loss in the Lithium-Rich Oxide $Li[Li_{1/5}Ni_{1/5}Mn_{3/5}]O_2$. *Journal of the Electrochemical Society*, **158**(6); A731

Wang, Y. X., K. H. Shang, W. He, X. P. Ai, Y. L. Cao, and H. X. Yang (2015). Magnesium-Doped $Li_{1.2}[Co_{0.13}Ni_{0.13}Mn_{0.54}]O_2$ for Lithium-Ion Battery Cathode with Enhanced Cycling Stability and Rate Capability. *ACS Applied Materials & Interfaces*, **7**(23); 13014–13021

Wu, F., J. Tian, Y. Su, Y. Guan, Y. Jin, Z. Wang, T. He, L. Bao, and S. Chen (2014). Lithium-Active Molybdenum Trioxide Coated $LiNi_{0.5}Co_{0.2}Mn_{0.3}O_2$ Cathode Material with Enhanced Electrochemical Properties for Lithium-Ion Batteries. *Journal of Power Sources*, **269**; 747–754

Xiang, M., C.-W. Su, L. Feng, M. Yuan, and J. Guo (2014). Rapid Synthesis of High-Cycling Performance $LiMg_xMn_{2-x}O_4$ ($x \leq 0.20$) Cathode Materials by a Low-Temperature Solid-State Combustion Method. *Electrochimica Acta*, **125**; 524–529

Yi, Z. (2016). Rheological Phase Reaction Synthesis of Co-Doped $LiMn_2O_4$ Octahedral Particles. *Journal of Materials Science: Materials in Electronics*, **27**; 10347–10352

Yuan, L.-X., Z.-H. Wang, W.-X. Zhang, X.-L. Hu, J.-T. Chen, Y.-H. Huang, and J. B. Goodenough (2011). Development and Challenges of $LiFePO_4$ Cathode Material for Lithium-Ion Batteries. *Energy & Environmental Science*, **4**(2); 269–284

Zhao, H., F. Li, X. Liu, W. Xiong, B. Chen, H. Shao, D. Que, Z. Zhang, and Y. Wu (2015). A Simple, Low-Cost and Eco-Friendly Approach to Synthesize Single-Crystalline $LiMn_2O_4$ Nanorods with High Electrochemical Performance for Lithium-Ion Batteries. *Electrochimica Acta*, **166**; 124–133

Zhu, Z. and L. Zhu (2014). Synthesis of Layered Cathode Material $0.5Li_2MnO_3{\cdot}0.5LiMn_{1/3}Ni_{1/3}Co_{1/3}O_2$ by an Improved Co-Precipitation Method for Lithium-Ion Battery. *Journal of Power Sources*, **256**; 178–182

Zipare, K., S. Bandgar, and G. Shahane (2018). Effect of Dy-Substitution on Structural and Magnetic Properties of MnZn Ferrite Nanoparticles. *Journal of Rare Earths*, **36**(1); 86–94

